NASA TECHNICAL NOTE

NASA TN D-3541

LONGITUDINAL AERODYNAMIC CHARACTERISTICS OF A TENSION SHELL ENTRY CONFIGURATION AT MACH 20

by Theodore R. Creel, Jr.

Langley Research Center
Langley Station, Hampton, Va.

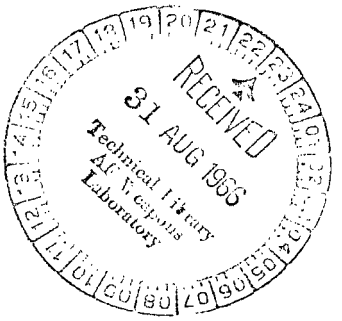

NATIONAL AERONAUTICS AND SPACE ADMINISTRATION • WASHINGTON, D. C. • AUGUST 1966

LONGITUDINAL AERODYNAMIC CHARACTERISTICS OF A TENSION SHELL ENTRY CONFIGURATION AT MACH 20

By Theodore R. Creel, Jr.

Langley Research Center
Langley Station, Hampton, Va.

NATIONAL AERONAUTICS AND SPACE ADMINISTRATION

For sale by the Clearinghouse for Federal Scientific and Technical Information
Springfield, Virginia 22151 – Price $2.00

LONGITUDINAL AERODYNAMIC CHARACTERISTICS OF A TENSION SHELL ENTRY CONFIGURATION AT MACH 20

By Theodore R. Creel, Jr.
Langley Research Center

SUMMARY

The aerodynamic characteristics of pointed and slightly blunted versions of a tension shell entry configuration were obtained at a Mach number of 20, a ratio of wall temperature to total temperature of approximately 0.1, and a Reynolds number of approximately 0.15×10^6 for an angle-of-attack range of 0^o to 45^o. Pressure distributions on the pointed configuration were obtained over an angle-of-attack range of 0^o to 15^o. The present investigation indicated that the pointed configuration was stable at all angles of attack, whereas neutral stability was exhibited at low angles of attack by the blunted configuration. Comparison with results from an earlier investigation at a Mach number of 6.74 revealed that an increase in Mach number did not affect the axial-force coefficient of the pointed configuration but decreased the stability and normal force of both configurations at low angles of attack. Increasing the Mach number increased the maximum axial-force coefficient and shifted the angle of attack at which maximum axial-force coefficient would occur on the blunted configuration. Newtonian theory predicted the pitching moments and normal forces for the present investigation with some degree of accuracy, but it yielded poor predictions for the axial force at low angles of attack for both configurations. The experimental pressure distributions obtained for the pointed configuration indicated that the assumption of a Newtonian pressure distribution is not valid.

INTRODUCTION

The entry of an unmanned probe into the low-density atmosphere of Mars requires a vehicle with high drag to dissipate the major portion of its kinetic energy before it strikes the surface of the planet and also to extend the dwell time of the vehicle within the atmosphere of the planet for the gathering and transmitting of data (ref. 1). A family of vehicles which has a high drag coefficient, a low structural weight, and a reasonable payload potential is discussed in detail in reference 2. These cusp-like configurations consist of a conical forebody which flares into a large base creating a large drag area. The flare is curved so that the aerodynamic forces will result only in tensile stresses in the shell of the structure; thus, the name of "tension shell" is given to the shape. The

payload for such a configuration would be contained in the conical forebody. Aerodynamic investigations have been conducted in wind tunnels on several tension shell configurations with variations in nose bluntness and length-diameter ratio. These results are presented in references 3 and 4 for a Mach number of about 7. It was of interest to determine the aerodynamic characteristics of the tension shell configuration at a Mach number of 20. Therefore, an investigation was conducted on pointed and slightly blunted versions of a tension shell configuration at a Mach number of 20 and a Reynolds number of approximately 0.15×10^6 in nitrogen over an angle-of-attack range of 0° to 45°. Normal force, axial force, and pitching moment were measured by a three-component strain-gage balance. The pressure over the pointed model was measured at angles of attack from 0° to 15° and was compared with Newtonian approximations (ref. 5). The measured force and moment coefficients were compared with Newtonian estimates and with unpublished data obtained by Peter T. Bernot in the Langley 11-inch hypersonic tunnel at a Mach number of 6.74 and a Reynolds number of approximately 0.16×10^6 in air.

SYMBOLS

The data are referred to the body axes and the stability axes which originate at a reference center of gravity located at a station 0.563 model-base radius from the model base on the center line. (See fig. 1.)

A model-base area, πr_b^2

C_A axial-force coefficient, $\frac{F_A}{q_\infty A}$

C_D drag coefficient, $\frac{F_D}{q_\infty A}$

C_L lift coefficient, $\frac{F_L}{q_\infty A}$

C_m pitching-moment coefficient, $\frac{M_Y}{2q_\infty r_b A}$

C_N normal-force coefficient, $\frac{F_N}{q_\infty A}$

C_p pressure coefficient, $\frac{p_S - p_\infty}{q_\infty}$

F_A axial force

F_D drag force, $F_N \sin \alpha + F_A \cos \alpha$

F_L lifting force, $F_N \cos \alpha - F_A \sin \alpha$

F_N normal force

l model length (see fig. 3)

L/D lift-drag ratio

M_Y pitching moment about model reference center of gravity (see fig. 1)

M_∞ free-stream Mach number

p pressure

p_∞ free-stream static pressure

q_∞ free-stream dynamic pressure

r radius

N_{Re} Reynolds number based on model maximum diameter, $\frac{\rho_\infty V_\infty 2r_b}{\mu_\infty}$

t elapsed tunnel test time

V_∞ free-stream velocity

x distance to orifice location (see fig. 3)

z axial distance on model (see fig. 2)

α angle of attack

μ_∞ free-stream absolute viscosity

ρ_∞ free-stream density

Subscripts:

b model base

S local model surface

max maximum

i arc-chamber conditions preceding arc discharge

t,1 arc-chamber conditions following arc discharge

t,2 stagnation conditions behind normal shock

FACILITY AND APPARATUS

Facility and Tests

The present investigation was conducted in nitrogen in the Langley hotshot tunnel, which is an arc-heated, hypervelocity, blowdown facility. The major components of the tunnel are a capacitor bank for storage of electrical energy, a 3000-cubic-centimeter arc chamber with coaxial electrodes, a 10° total-divergence-angle conical nozzle and test section followed by a 60.96-centimeter-diameter cylindrical section, a 10° cone-cylinder diffuser, and a 8.496-cubic-meter vacuum chamber. A complete description and a calibration of the facility are presented in reference 6.

In this investigation, the tunnel was operated at a free-stream Mach number of 20 and at a Reynolds number based on model-base diameter of approximately 0.15×10^6. The nominal arc-chamber stagnation temperature and pressure were 2500° K and 68.9 MN/m^2. The ratio of wall temperature to total temperature was approximately 0.1. The angle-of-attack range was 0° to 45° for the force tests and 0° to 15° for the pressure test.

Models

The force models, A (pointed) and B (slightly blunted), are shown in figure 2. These models were fabricated by wrapping layers of fiber glass over a mold and bonding the layers with an epoxy resin. This thin-wall minimum-mass construction helped to minimize the moments of inertia of the model-balance system and insured that the natural

frequency of the model-support-balance system would be as high as possible; thus, vibrations could be damped in order to obtain acceptable measurements during the 0.1-second test time. The construction of the pressure model (shown in fig. 3) was the same as that of the force models except that mass was not a consideration; therefore, the walls of the pressure model are thicker and provide support for the pressure tubes and transducers.

Instrumentation

Pressure measurements.- The short test time of the tunnel (approximately 0.1 second) required pressure transducers with very short response times, high sensitivity, and a minimum length of orifice tubing. These requirements were met by using a wafer-style variable-reluctance transducer. (See ref. 7 for description and theory of operation.) A typical pressure transducer installation and a common manifold are shown in figure 3. Orifices were provided for 20 measurements, but because of limited transducer space, only 15 were used. The orifices were arranged in two rays, 180° apart. The model was oriented in the tunnel so that the orifices were in the model pitch plane. The initial charge pressure in the arc chamber was measured with a Bourdon gage and after arc discharge, the arc-chamber stagnation pressure was measured with two high-response strain-gage transducers.

Force and moment measurements.- The aerodynamic forces and moments were measured by a three-component strain-gage balance (fig. 4) mounted in the model. This balance is very small and has certain unique structural features. These features include the construction and arrangement of the force and moment beams. The normal-force and pitching-moment beams consist of the elements of an I-beam as shown in figure 4. The pitching-moment strain gages are located on the horizontal flanges (section A-A) and the axial-force strain gages, on the vertical webs that connect the two major parts of the balance (section B-B).

Data acquisition.- Outputs from the strain gages and the pressure transducers were amplified with 3-kilocycle and 20-kilocycle carrier amplifiers, respectively, and were then recorded on oscillographs. A representative oscillograph record from the present investigation is shown as figure 5. In addition to the high quality of the force and pressure traces in figure 5, it can be noted that the tunnel starting transients were only a small part of the total run time.

DATA REDUCTION AND ACCURACY

The measured arc-chamber pressure, the test-section pitot pressure, and the calculated arc-chamber density were used as inputs to the real nitrogen data-reduction program of reference 8. This program considers intermolecular forces in the arc chamber,

but it does not consider any vibrational nonequilibrium that may exist in the test-section flow.

Uncertainties involved in the instrumentation, the resolution of oscillograph records, and the repeatability of test conditions caused maximum probable inaccuracies in the present data as follows:

C_N	±0.028
C_A	±0.017
C_m	±0.004
C_p	±0.02
M_∞	±0.5
α, deg	±0.1

RESULTS AND DISCUSSION

General Flow Field

Schlieren photographs of model B at an angle of attack of 0° are shown in figure 6. It may be inferred from the schlieren photograph (fig. 6(b)) that the bow shock extends back approximately one-half the body length and intersects the nearly normal detached shock wave which originates ahead of the flared skirt where the body slope exceeds the maximum turning that the stream can support. Flow separation over these bodies can be induced by nose bluntness (ref. 4) and by increasing the ratio of wall temperature to total temperature (ref. 9). The extent of separation in the flow field about the tension shell configuration would be expected to have a significant effect upon the drag coefficients at an angle of attack of 0°. Reference 4 shows that with increasing flow separation over the bow section of the model the drag coefficient decreased to a value much lower than that associated with completely attached flow. Therefore, the tension shell can have a high- or a low-drag flow regime. Figure 6 indicates that the flow is not separated and, thus, the body is probably in the high-drag flow regime for the present investigation. Schlieren photographs of model A were not of sufficient quality to be presented in this report. In figure 7(a), the photographs of model B at an angle of attack of 0° are assumed to illustrate the flow field which is typical for this type of body. The light area on the base of the model is believed to be caused by a high heating rate which charred the surface. This charred matter was then assumed to be eroded by the stream flow. (The surface contour was not sufficiently altered by the erosion to affect aerodynamic characteristics.) Reference 8 states that the heating rate on the base is much higher than that on the forebody of a concave model such as the tension shell configuration.

The flow field about model B at an angle of attack of 20° can be deduced from figure 7(b). The effect on the surface heating of the model caused by the intersection of the bow shock wave with the normal shock is indicated by the definite separation of light and dark areas which curve around the model and disappear on the leeward side. This separation is probably due to the separated boundary layer.

Longitudinal Characteristics

The longitudinal aerodynamic characteristics of models A and B are presented in figure 8. The Newtonian estimates of the force and moment coefficients for the two models were obtained for a $C_{p,max}$ of 2 by a computer program incorporating a calculation procedure based on the method described in reference 5, which neglects shielding effects.

The normal-force coefficients for models A and B (fig. 8(a)) are approximately the same for all angles of attack. The trends of both the experimental and the theoretical results are similar, but the Newtonian approximations overpredict the experimental normal-force coefficients at angles of attack greater than 15°.

The axial-force coefficients for the two models are approximately the same for all angles of attack greater than 15°, with maximum values occurring at angles of attack of of 0° and 2.5° for models A and B, respectively. At an angle of attack of 0°, the flow is apparently attached to the forebody of model A and causes a higher axial-force coefficient (fig. 8(a)) than that exhibited by model B. As the angle of attack is increased, the flow begins to separate from the leeward side of model A, but it does not detach from the windward side. The separation on the leeward side causes a gradual decrease in the axial-force coefficient. The flow field about model B is slightly separated at an angle of attack of 0° and, as discussed in the section "General Flow Field," this slightly separated flow causes a decrease in axial-force coefficient. As the angle of attack is increased, the extent of flow separation increases on the leeward side but decreases on the windward side; as a result, the axial-force coefficient is increased. The axial-force-coefficient curves merge at an angle of attack of about 2.5° and follow the same decreasing trend. The Newtonian values of the axial-force coefficient are much less than the experimental values until the angle of attack reaches about 30°, at which point the flow is completely separated from the leeward side of the models.

The experimental pitching-moment coefficients taken about a point 0.563 model-base radius from the model base are generally predicted by Newtonian approximations. The experimental data indicate that model A has nearly constant stability throughout the angle-of-attack range. Model B is almost neutrally stable to an angle of attack of about 2.5°, after which there is a sudden increase in stability. This sudden increase in stability is

attributed to flow separation on the leeward side and flow attachment on the windward side, shifting the center of pressure rearward. Neutral stability is exhibited by model B at angles of attack between approximately 5° and 20°, after which the model becomes stable.

The experimental longitudinal aerodynamic characteristics referred to the stability axes are presented in figure 8(b) along with the Newtonian approximations. The maximum drag coefficient of 1.6 occurs at an angle of attack of 0° for model A and the maximum drag coefficient of 1.52 occurs at an angle of attack of approximately 2.5° for model B. The trends of the Newtonian approximations and the experimental drag coefficients are quite different, with Newtonian theory predicting a much smaller drag coefficient until an angle of attack of about 30°, after which the theoretical and experimental trends are approximately the same. Newtonian theory was not expected to predict these results because of the two intersecting flow fields. One other method (ref. 10) was considered to approximate the experimental data, but the results were much worse than Newtonian approximations.

The experimental lift coefficient for both models exhibited the same trend as theory, but at an angle of attack of approximately 20° a large discrepancy between theoretical and experimental lift coefficients is observed. The experimental and theoretical lift-drag-ratio curves are similar.

A comparison of the data from the present investigation with previously unpublished results obtained in the Langley 11-inch hypersonic tunnel by Peter T. Bernot at a Mach number of 6.74, a Reynolds number of 0.16×10^6, and a ratio of wall temperature to total temperature of 0.5 is presented in figure 9. In the comparison, no consideration is given to the difference in ratio of wall temperature to total temperature between the two investigations. Figure 9(a) indicates that for model A the normal force is higher at a Mach number of 6.74 than at a Mach number of 20 until an angle of attack of about 15°, after which the normal-force coefficients for both Mach numbers are essentially the same. There is good agreement between the axial-force coefficients of model A at the two Mach numbers. The increase in Mach number caused a decrease in stability at low angles of attack. However, after an angle of attack of about 17°, the stability of model A was approximately the same for both Mach numbers.

Figure 9(b) indicates that for model B at a Mach number of 6.74, the axial-force coefficient at an angle of attack of 0° is lower than that at a Mach number of 20. Also, the maximum axial-force coefficient occurs at an angle of attack of approximately 6° for a Mach number of 6.74 and at an angle of attack of approximately 2.5° for a Mach number of 20. Increasing the Mach number from 6.74 to 20 decreases the stability of model B at low angles of attack, after which it follows the same general trend as model A.

Pressure Distribution

The experimental pressure distributions for model A with Newtonian approximations for angles of attack from 0° to 15° are shown in figure 10. At an angle of attack of 0° (fig. 10(a)), the experimental pressure coefficients follow the Newtonian trend until the value of x/l reaches about 0.6; then, the pressure coefficient increases sharply because of the presence of the nearly normal shock. At angles of attack of 5° and 15° (figs. 10(b) and 10(d)), the experimental pressure coefficients increase on the windward side while they decrease on the leeward side. There are several points in figures 10(b) and 10(d) that do not follow the general trend of the experimental pressure coefficients. These points are probably caused by the reflected shocks within the flow field (as seen in fig. 5(b) of ref. 3 for $\alpha = 6^{\circ}$) striking the surface of the model in the region of the pressure orifices. The experimental pressure coefficients at an angle of attack of 10° (fig. 10(c)) do not follow the diverging trend of the windward and leeward pressure coefficients at the other angles of attack because of the reflected shocks, as was previously discussed. Newtonian theory, in general, does not adequately predict pressure distribution for this configuration.

CONCLUSIONS

Longitudinal aerodynamic characteristics of pointed and slightly blunted versions of a tension shell entry configuration and pressure distributions of a pointed version of a tension shell entry configuration were investigated at a Mach number of 20, a Reynolds number of approximately 0.15×10^6 over an angle-of-attack range of 0° to 45°, and a ratio of wall temperature to total temperature of 0.1. Comparison of this information with the Newtonian approximations and with unpublished data from an earlier investigation at a Mach number of 6.74 was made. This study has led to the following conclusions:

1. The pointed configuration for a center-of-gravity location of 0.563 model-base radius from model base was stable at all angles of attack, whereas neutral stability was exhibited at low angles of attack by the blunted configuration.

2. At the higher Mach number, the axial-force coefficient of the pointed configuration was unaffected, but the stability and the normal force were decreased at low angles of attack.

3. An increase in Mach number decreased the stability of the blunted configuration at low angles of attack.

4. Increasing the Mach number from 6.74 to 20 increased the maximum axial-force coefficient and shifted the angle of attack at which maximum axial-force coefficient would occur on the blunted configuration.

5. Newtonian theory predicted the pitching moment and the normal force with some degree of accuracy, but it yielded poor predictions for axial force at low angles of attack for either configuration.

6. In general, Newtonian theory did not adequately predict the pressure distributions for the pointed configuration.

Langley Research Center,
National Aeronautics and Space Administration,
Langley Station, Hampton, Va., May 11, 1966.

REFERENCES

1. Roberts, Leonard: Entry Into Planetary Atmospheres. Astronaut, Aeron., vol. 2, no. 10, Oct. 1964, pp. 22-29.

2. Anderson, Melvin S.; Robinson, James C.; Bush, Harold G.; and Fralich, Robert W.: A Tension Shell Structure for Application to Entry Vehicles. NASA TN D-2675, 1965.

3. Bernot, Peter T.: Longitudinal Stability Characteristics of Several Proposed Planetary Entry Vehicles at Mach 6.73. NASA TN D-2785, 1965.

4. Robinson, James C.; and Jordan, Alfred W.: Exploratory Experimental Aerodynamic Investigation of Tension Shell Shapes at Mach 7. NASA TN D-2994, 1965.

5. Rainey, Robert W.: Working Charts for Rapid Prediction of Force and Pressure Coefficients on Arbitrary Bodies of Revolution by Use of Newtonian Concepts. NASA TN D-176, 1959.

6. Miller, Charles G., III; Creel, Theodore R., Jr.; and Smith, Fred M.: Calibration Experience in the Langley Hotshot Tunnel for Mach Numbers From 12 to 26. NASA TN D-3278, 1966.

7. Smotherman, W. E.; and Maddox, W. V.: Variable Reluctance Pressure Transducer Development. AEDC-TDR-63-135, U.S. Air Force, July 1963.

8. Grabau, Martin; Humphrey, Richard L.; and Little, Wanda J.: Determination of Test-Section, After-Shock, and Stagnation Conditions in Hotshot Tunnels Using Real Nitrogen at Temperatures From 3000 to 4000^{o} K. AEDC-TN-61-82, U.S. Air Force, July 1961.

9. Centolanzi, Frank L.: Heat Transfer to Blunt Conical Bodies Having Cavities to Promote Separation. NASA TN D-1975, 1963.

10. Seiff, Alvin: Secondary Flow Fields Embedded in Hypersonic Shock Layers. NASA TN D-1304, 1962.

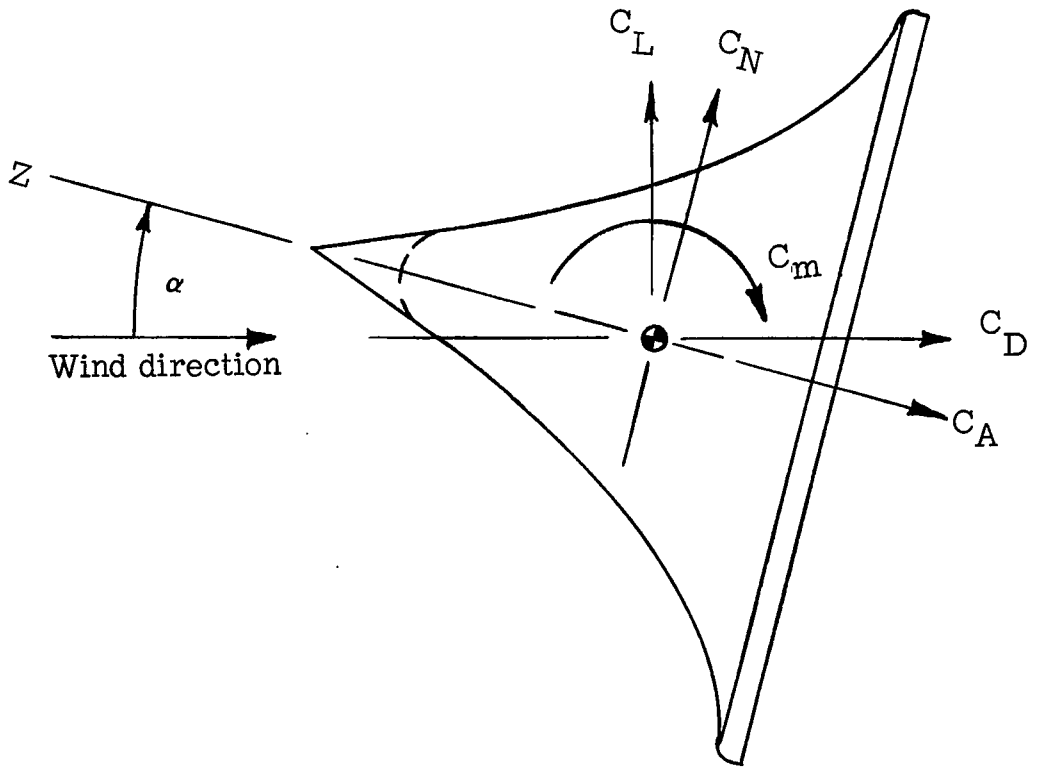

Figure 1.- Sketch of model showing positive direction of force and moment coefficients, angle of attack, and axes.

r_b = 1.5 inches (3.81 cm)

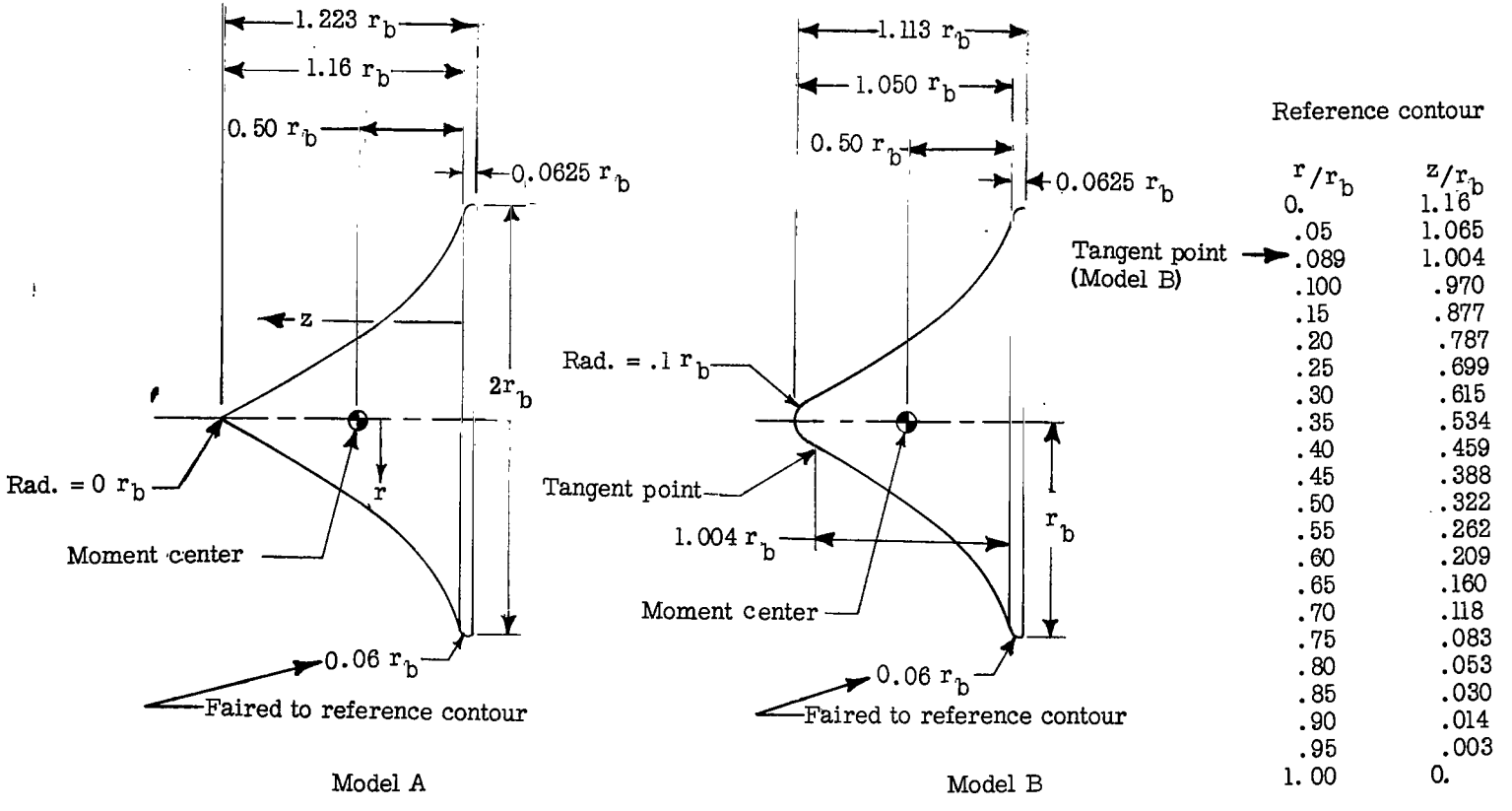

Reference contour

r/r_b	z/r_b
0.	1.16
.05	1.065
Tangent point (Model B) → .089	1.004
.100	.970
.15	.877
.20	.787
.25	.699
.30	.615
.35	.534
.40	.459
.45	.388
.50	.322
.55	.262
.60	.209
.65	.160
.70	.118
.75	.083
.80	.053
.85	.030
.90	.014
.95	.003
1.00	0.

Figure 2.- Geometry of force models used in present investigation.

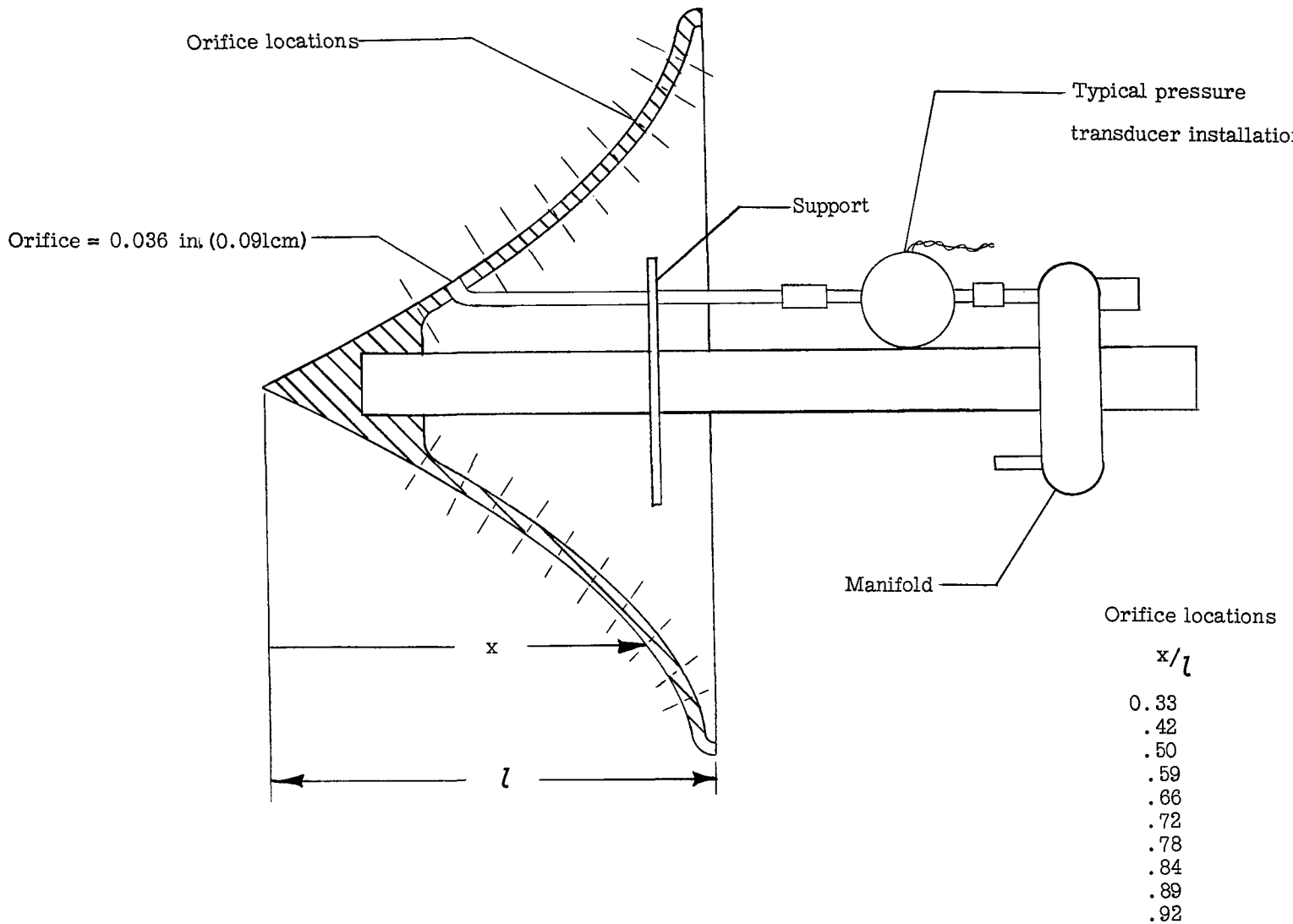

Figure 3.- Pressure model A used in present investigation; l = 1.834 inches (4.658 cm).

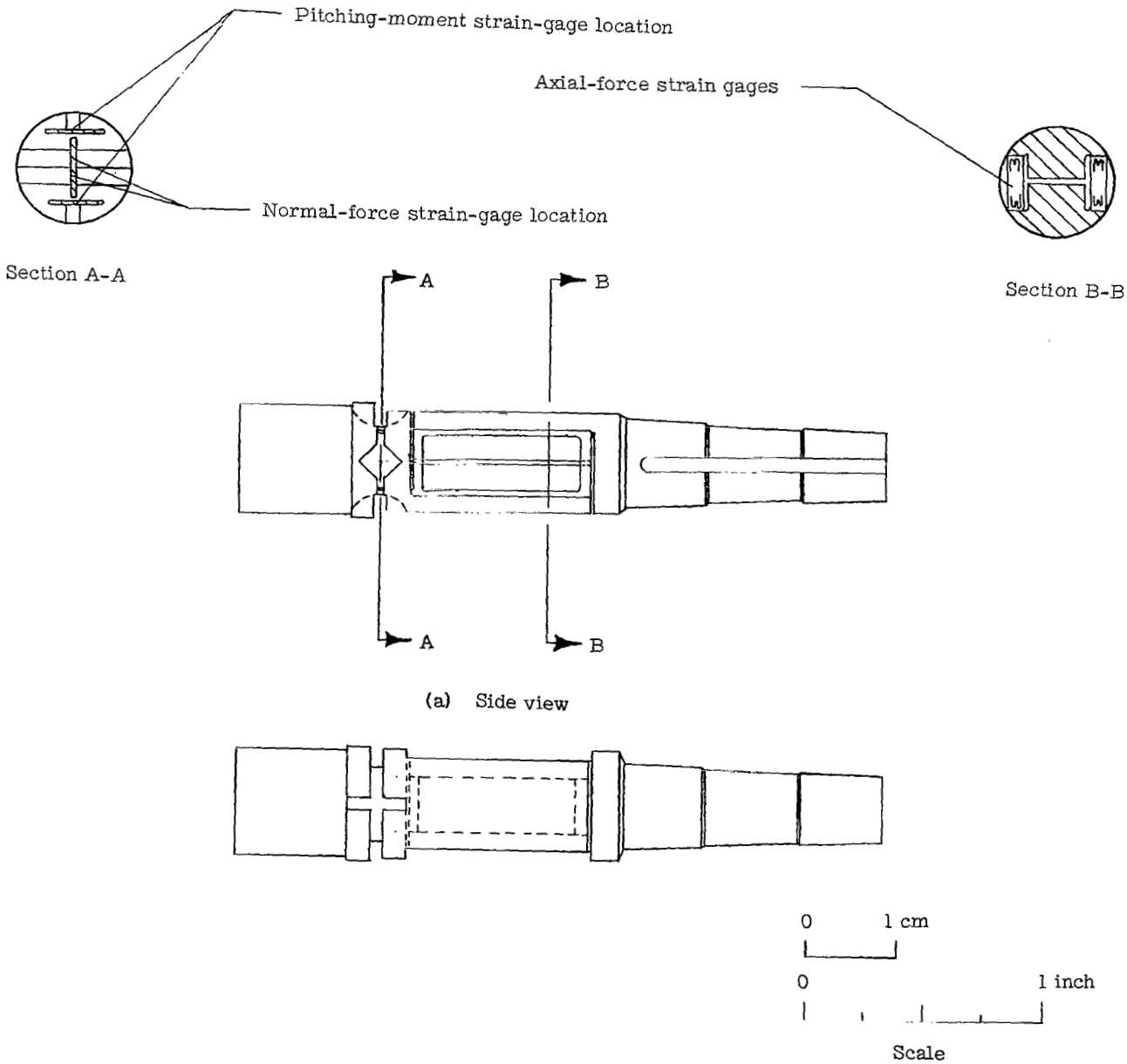

Figure 4.- Three-component strain-gage balance used in present investigation.

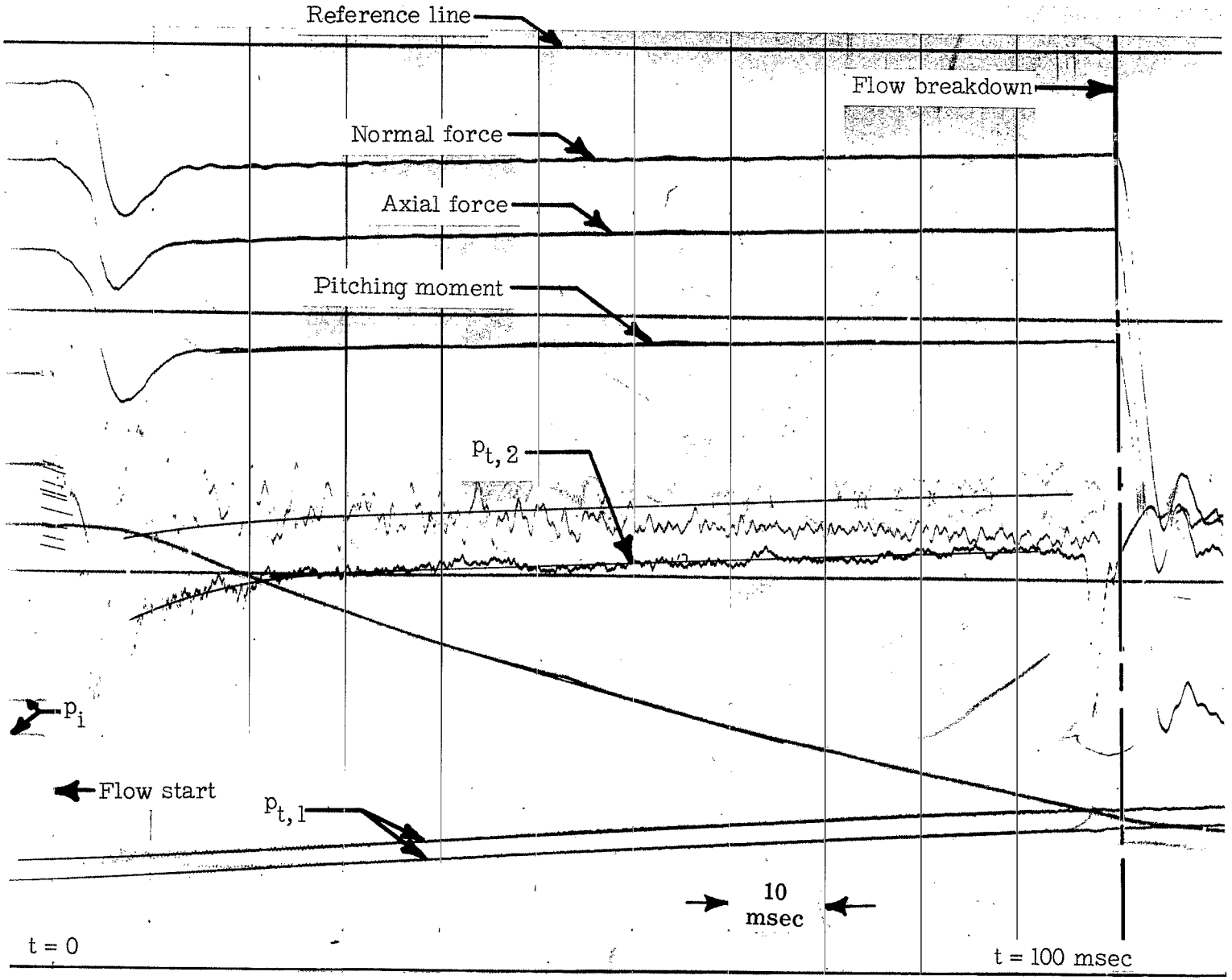

Figure 5.- Representative oscillograph record of pressure, force, and moment traces.

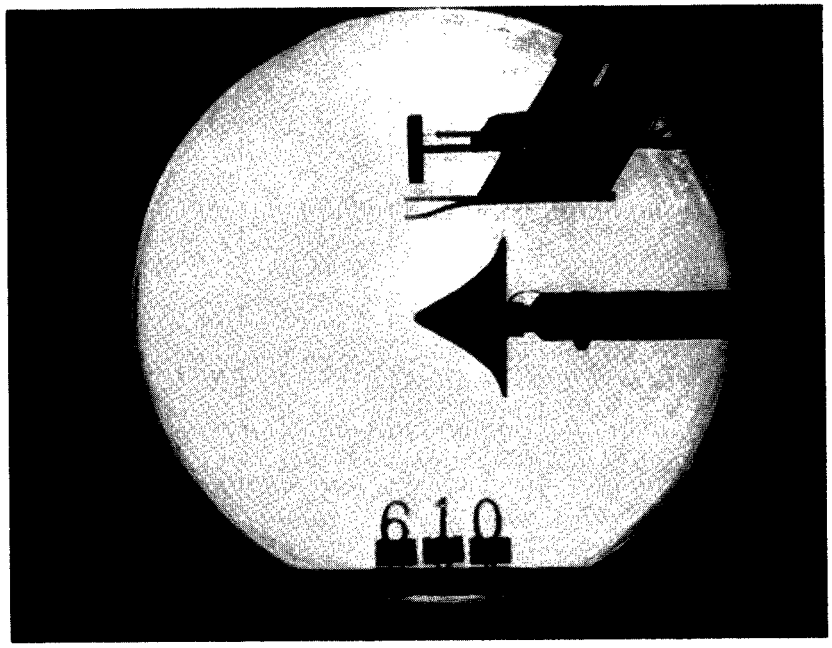

(a) No flow.

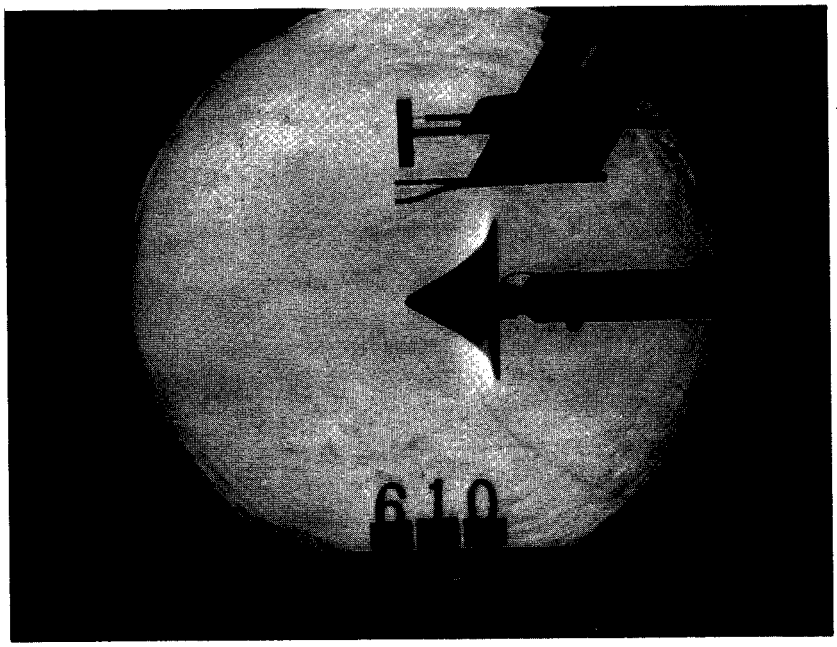

(b) Flow. L-66-1197

Figure 6.- Schlieren photographs of model B at $\alpha = 0^{0}$; $M_{\infty} = 20$; $N_{Re} \approx 1.5 \times 10^{6}$.

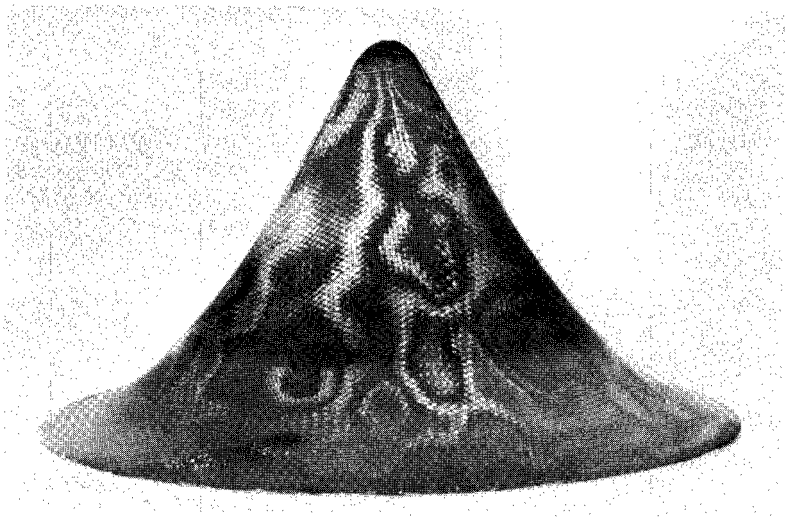

Side view

L-65-5053

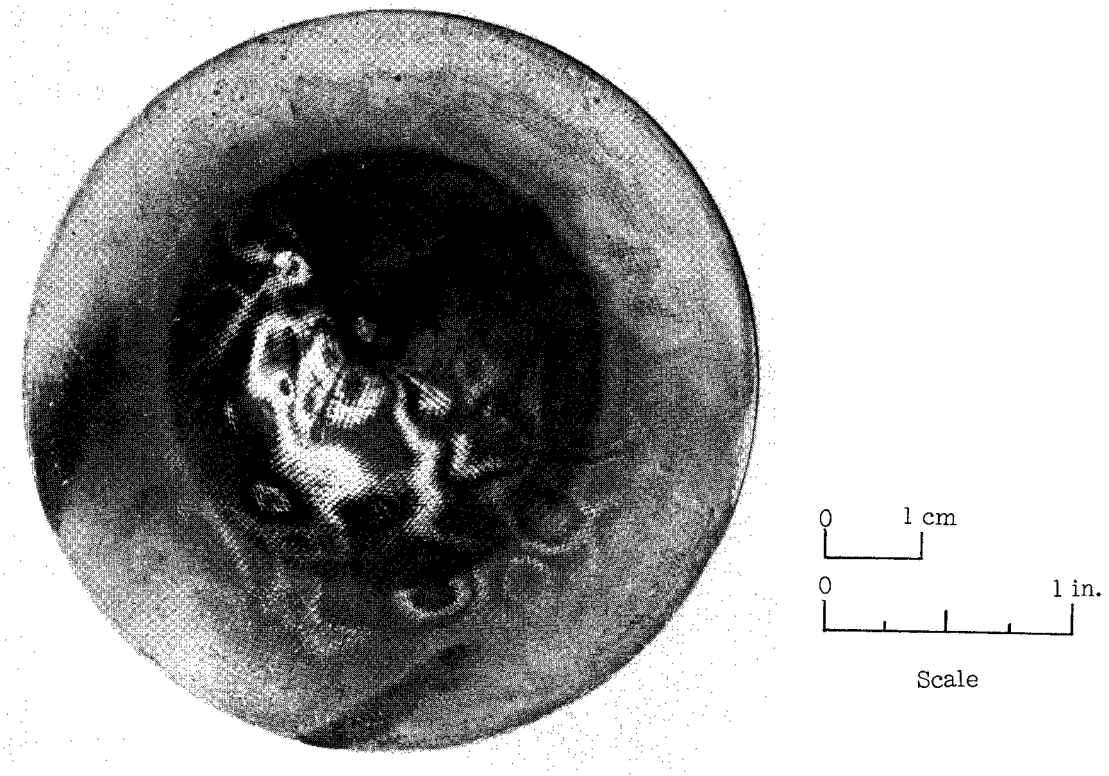

Front view

(a) Model B at $\alpha = 0^{\circ}$.

L-65-5055

Figure 7.- Photographs of model B used in present investigation.

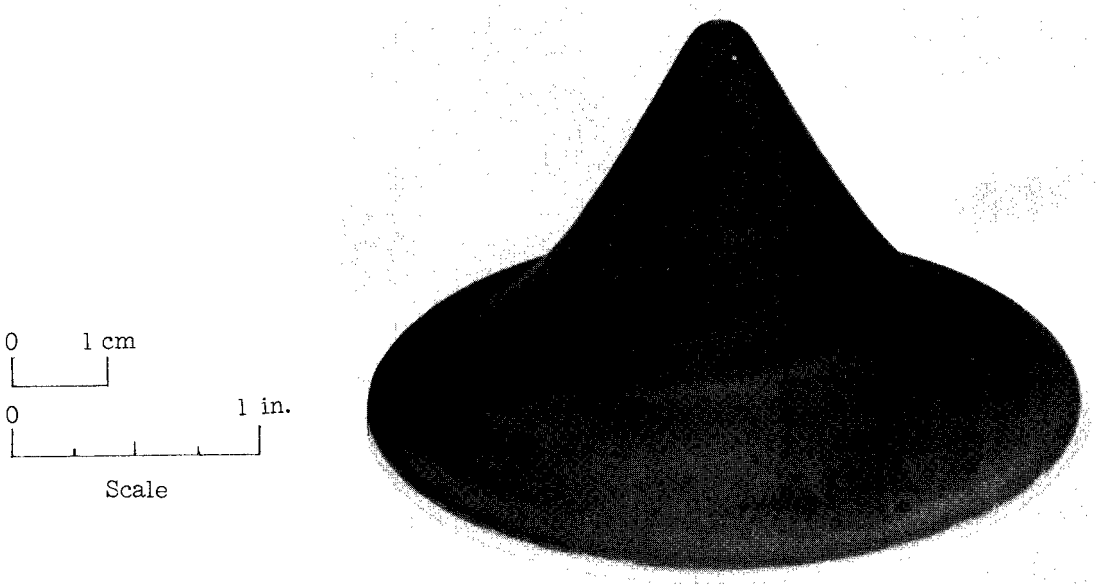

L-65-4852

Side view

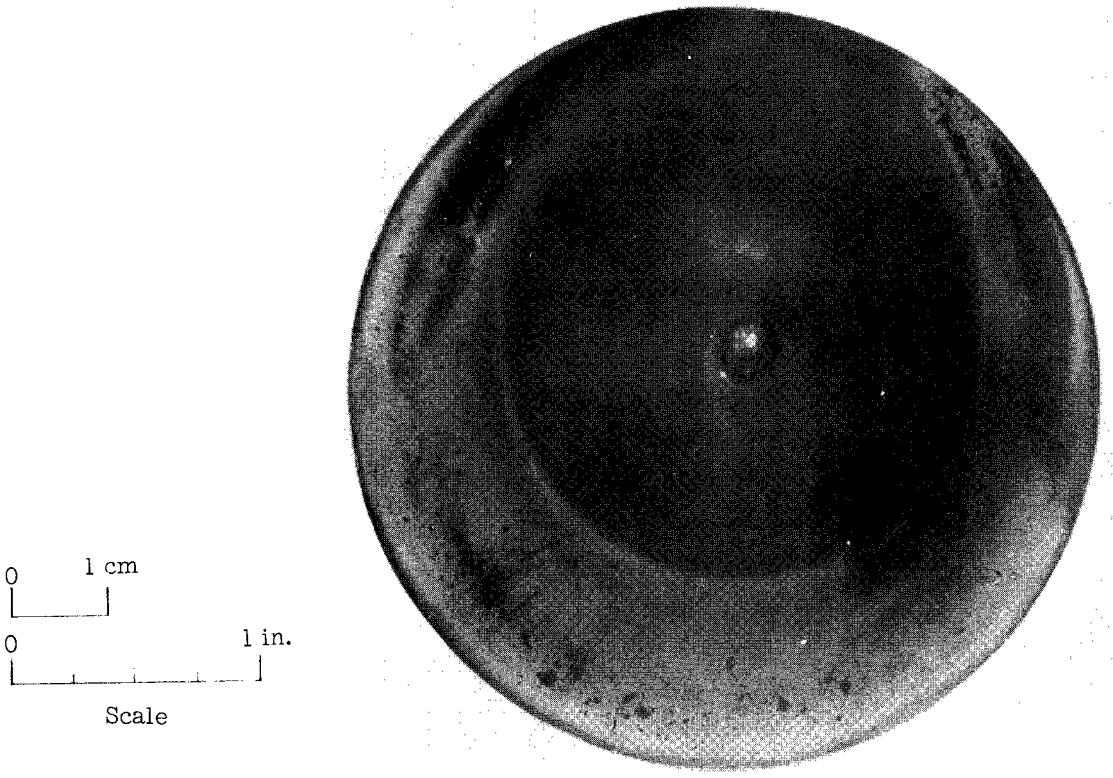

Front view.

(b) Model B at $\alpha = 20^{0}$.

L-65-4851

Figure 7.- Concluded.

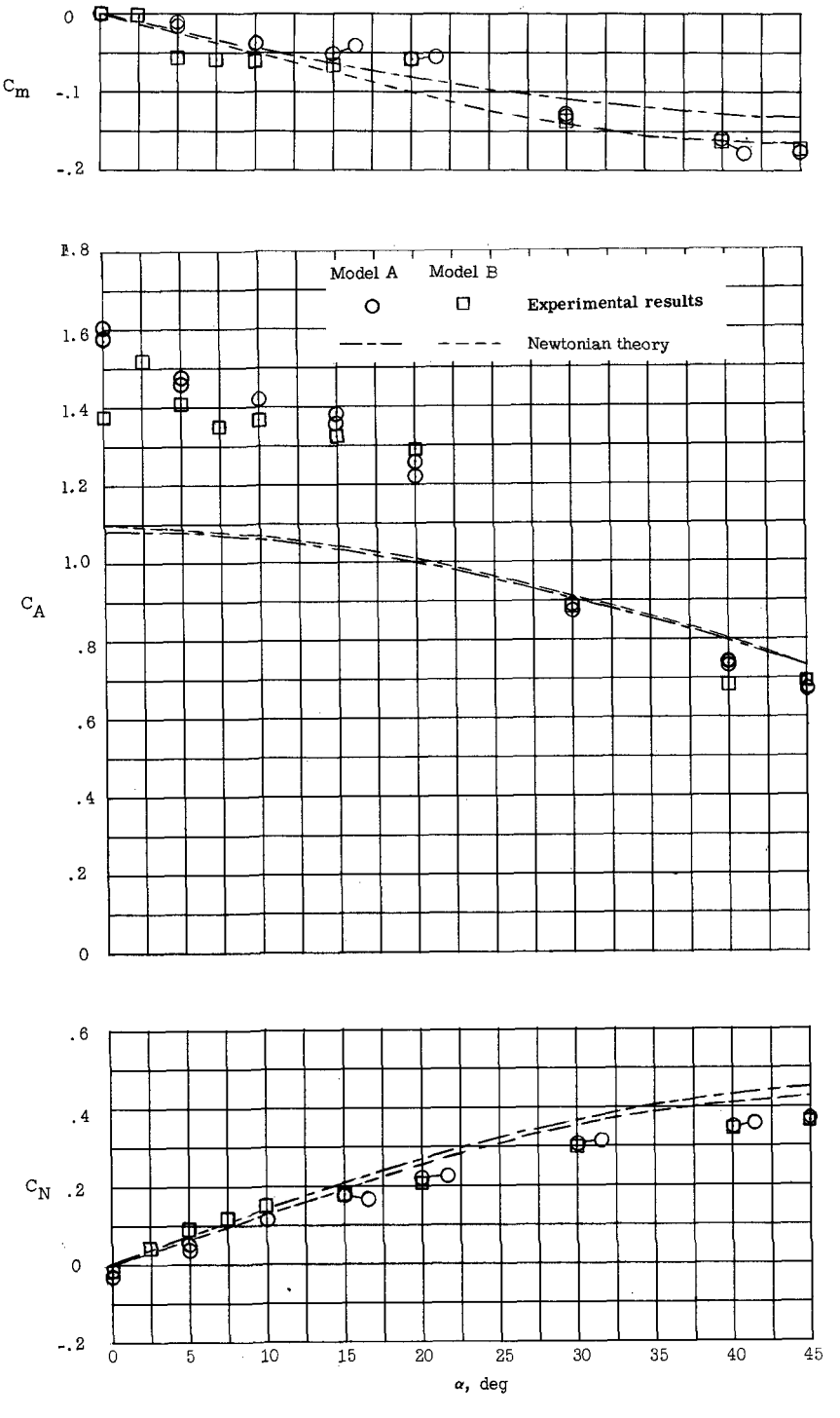

(a) Referred to body axis.

Figure 8.- Longitudinal aerodynamic characteristics of models at $M_\infty = 20$; $N_{Re} \approx 0.15 \times 10^6$.

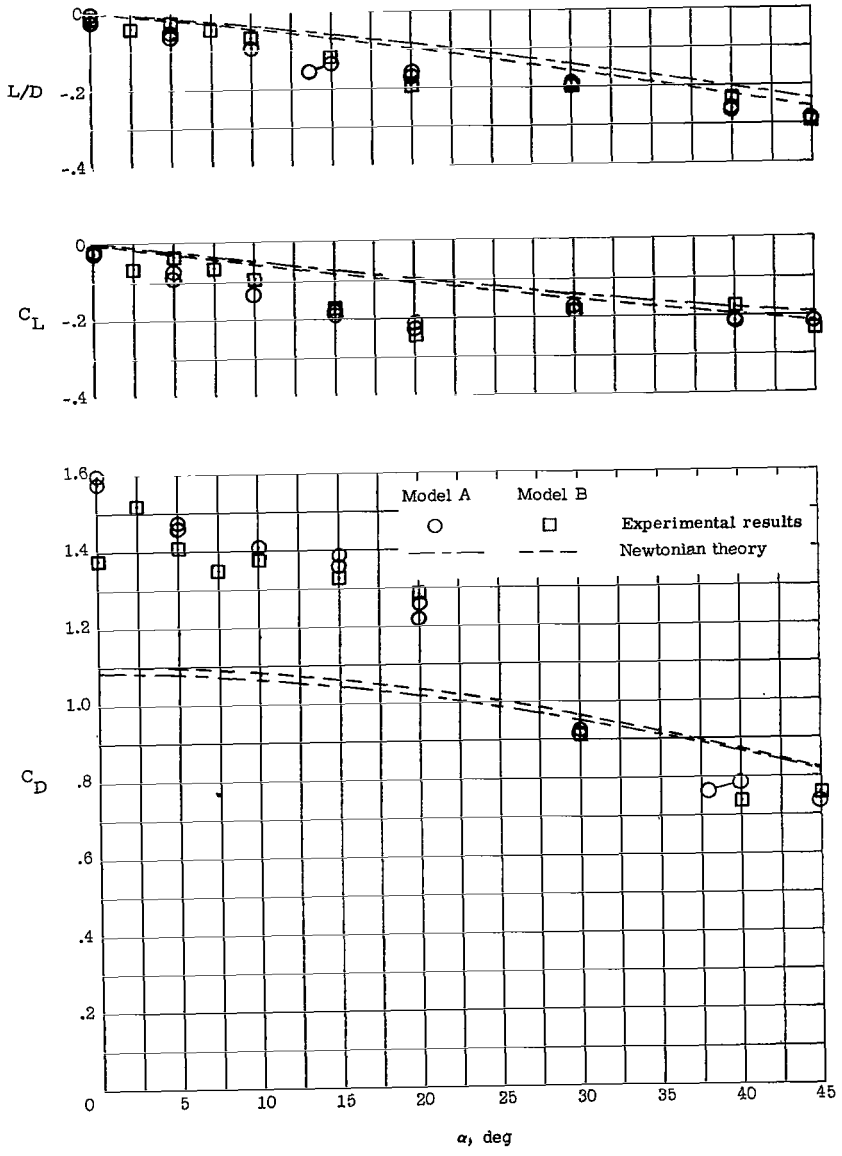

(b) Referred to the stability-axis system.

Figure 8.- Concluded.

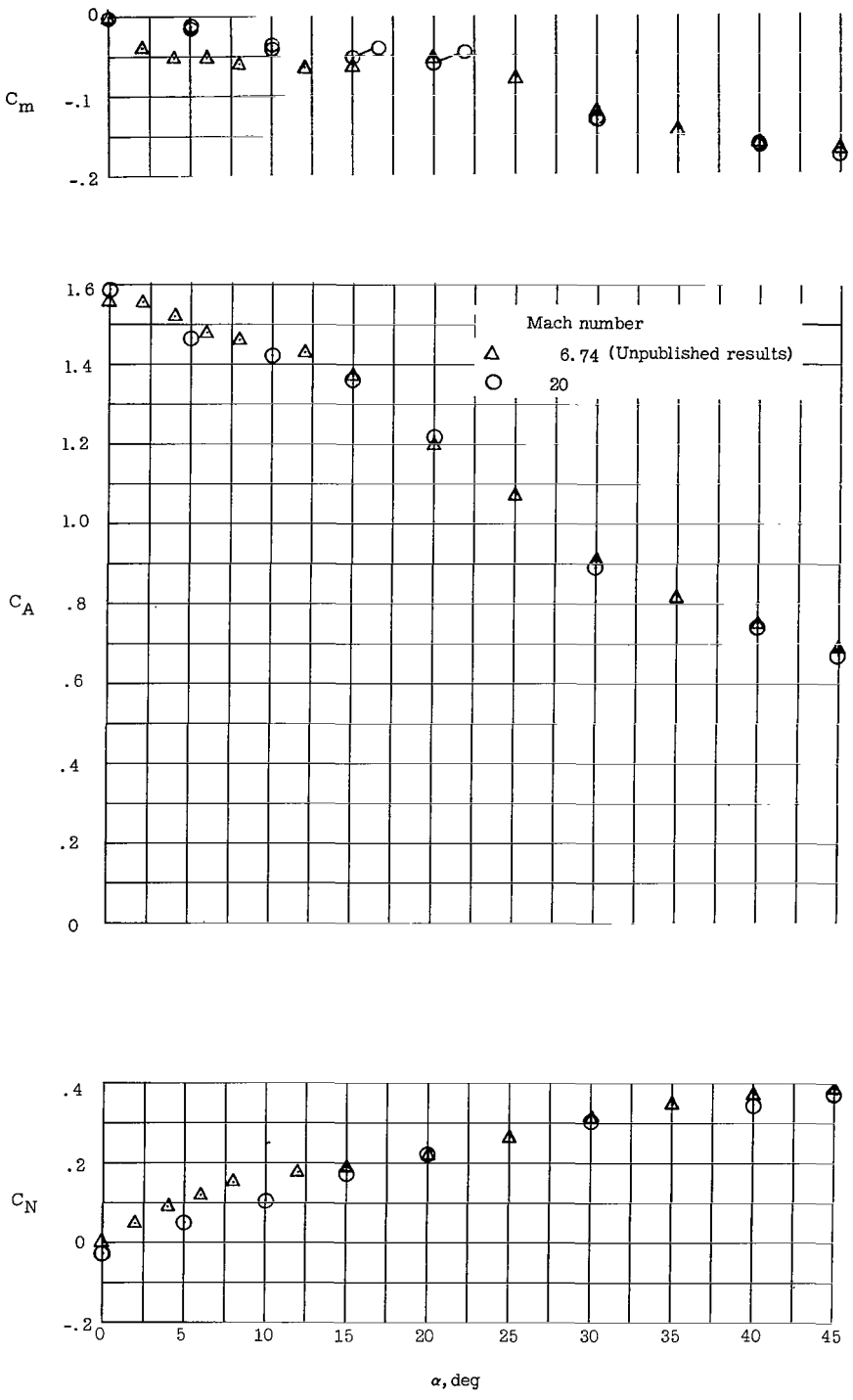

(a) Model A.

Figure 9.- Aerodynamic characteristics of models at $M_\infty = 6.74$ and 20; $N_{Re} \approx 0.15 \times 10^6$.

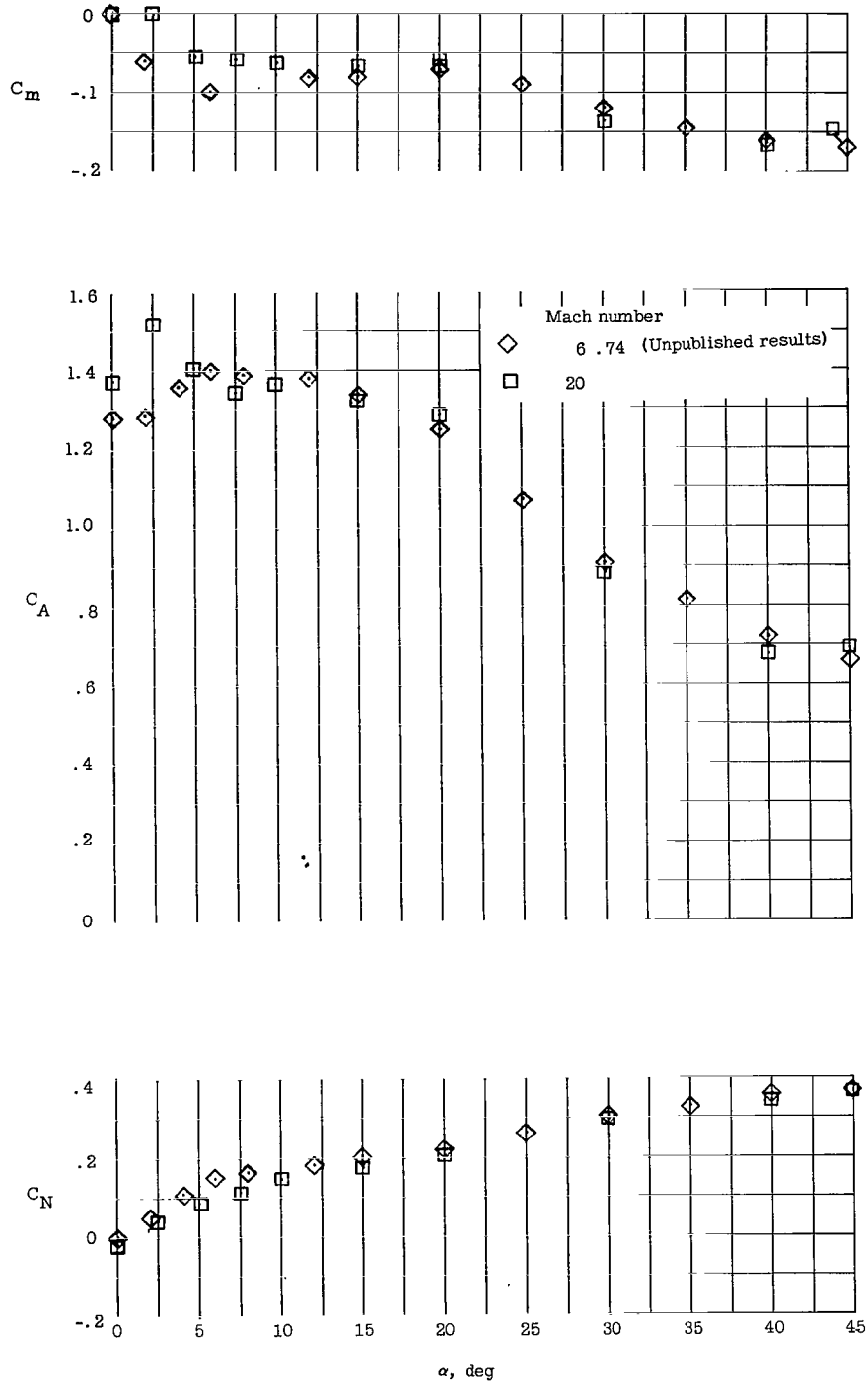

(b) Model B.

Figure 9.- Concluded.

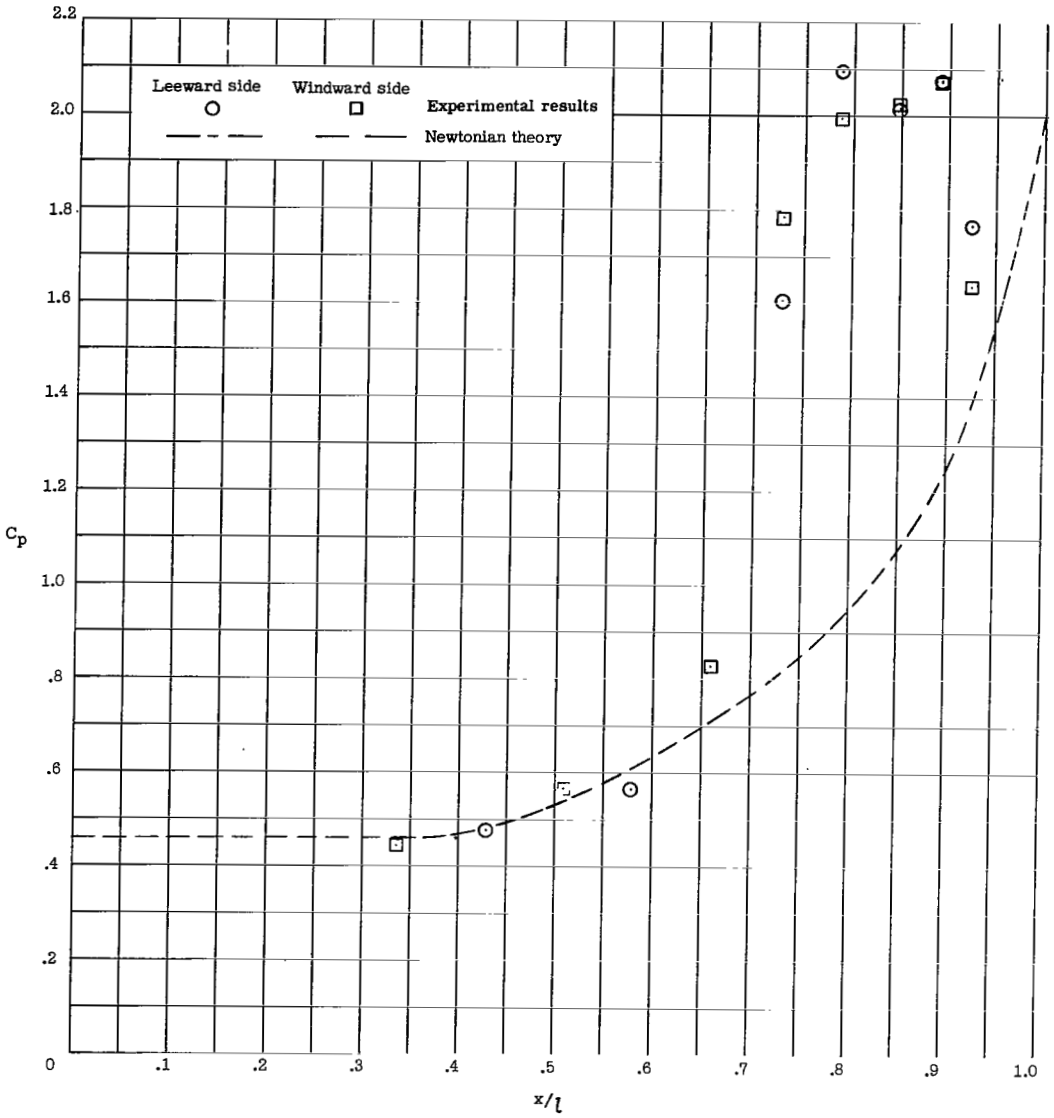

(a) $\alpha = 0^0$.

Figure 10.- Pressure distribution on model A, $M_\infty = 20$; $N_{Re} \approx 0.15 \times 10^6$.

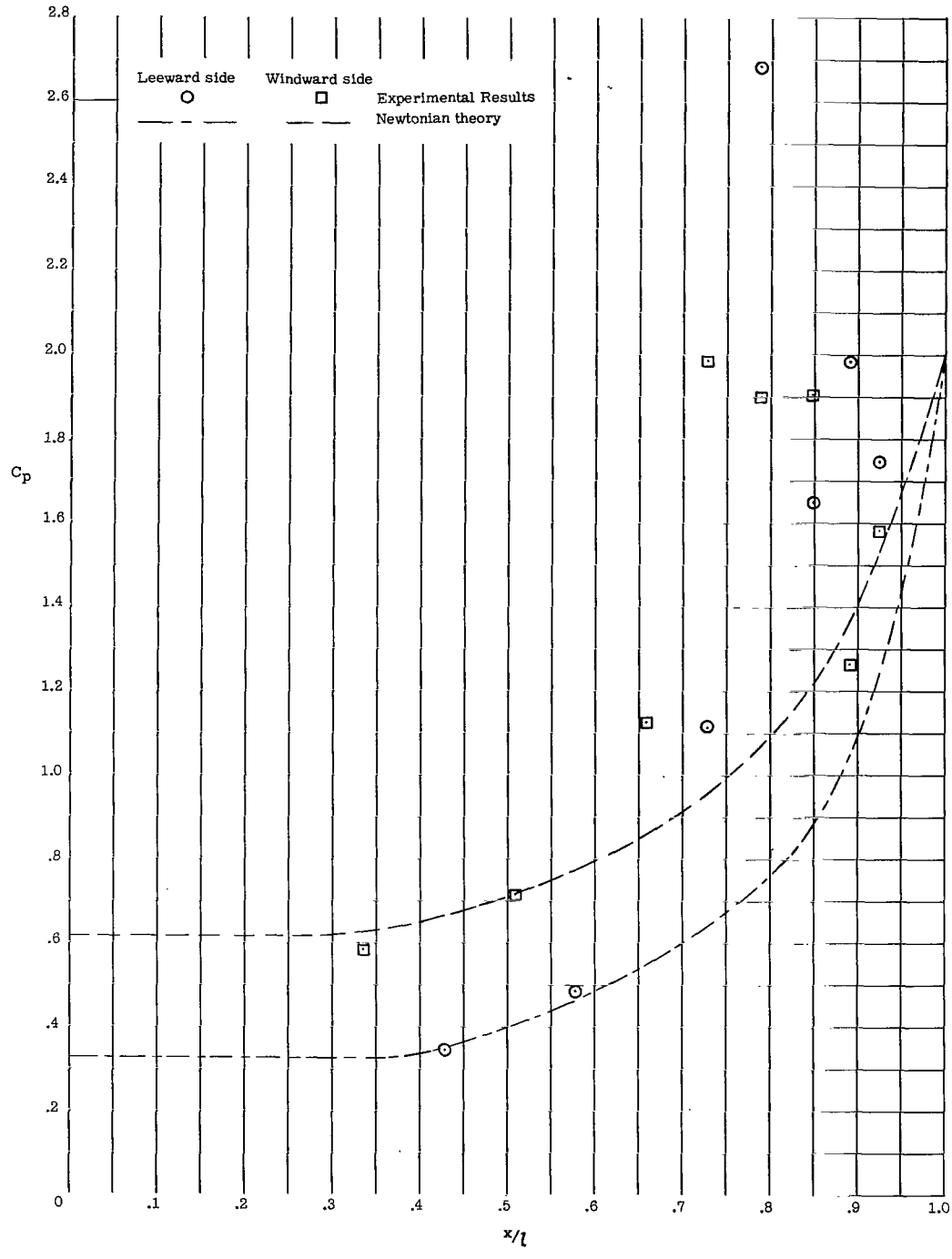

(b) $\alpha = 5^0$.

Figure 10.- Continued.

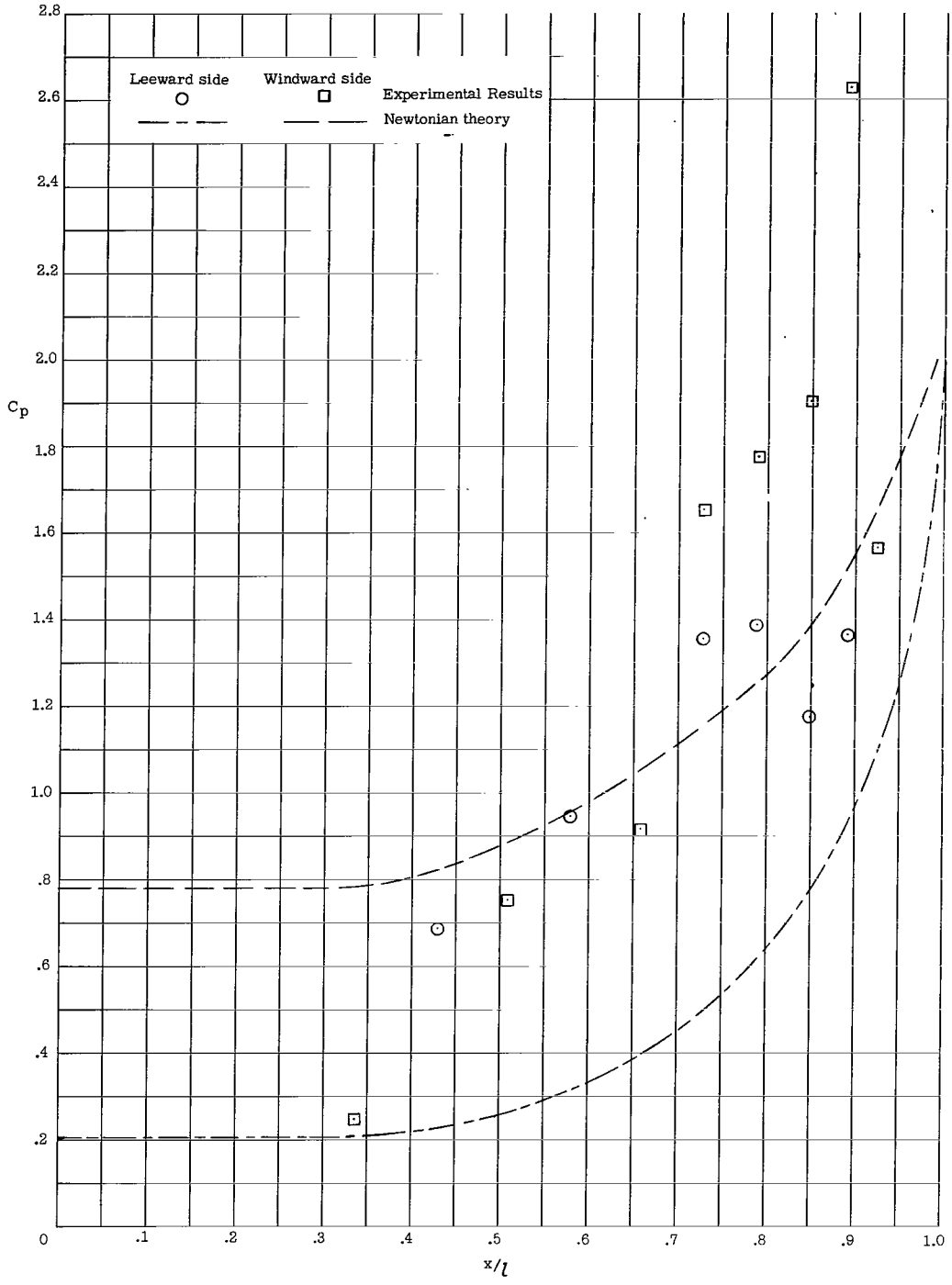

(c) $\alpha = 10^0$.

Figure 10.- Continued.

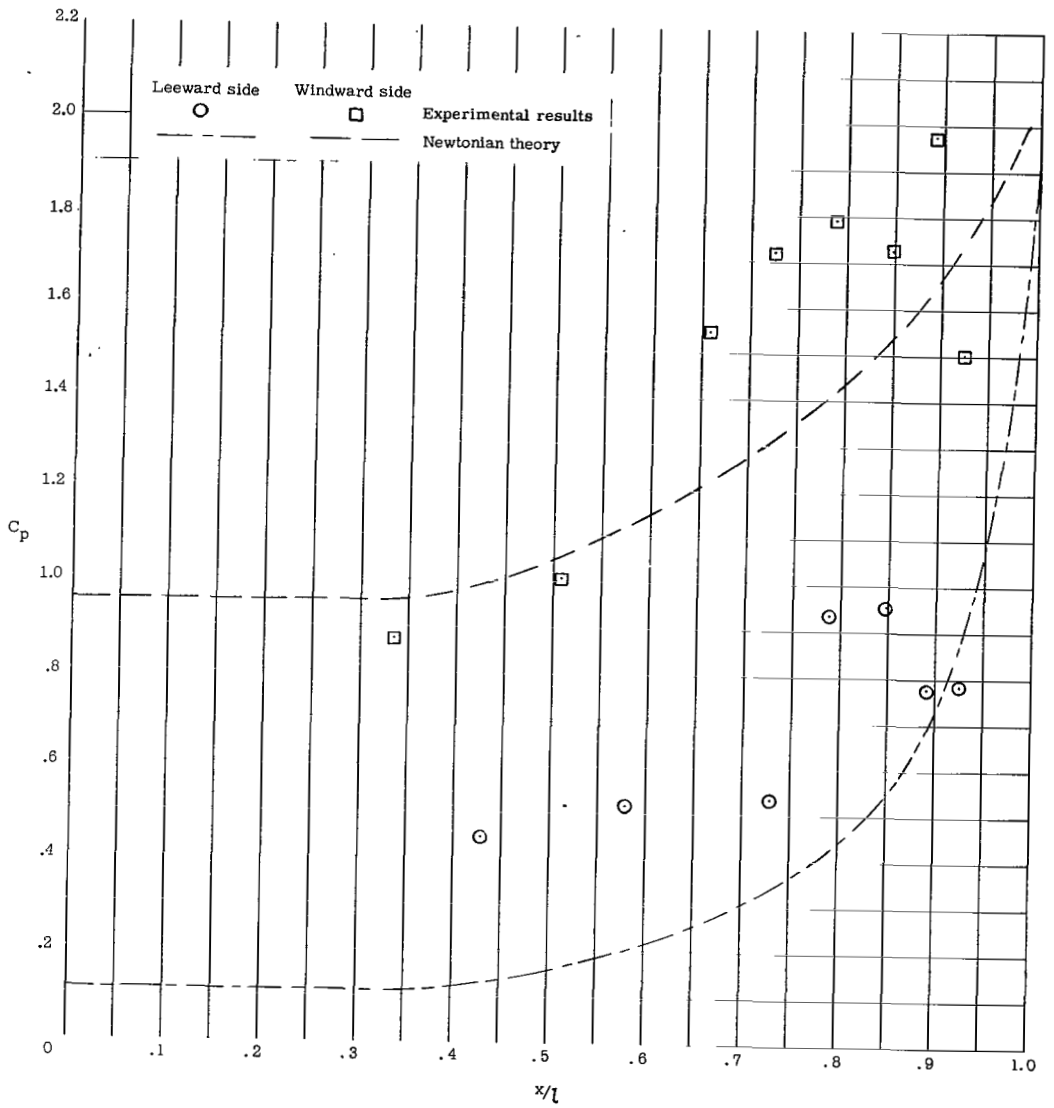

(d) $\alpha = 15^0$.

Figure 10.- Concluded.

"The aeronautical and space activities of the United States shall be conducted so as to contribute . . . to the expansion of human knowledge of phenomena in the atmosphere and space. The Administration shall provide for the widest practicable and appropriate dissemination of information concerning its activities and the results thereof."

—NATIONAL AERONAUTICS AND SPACE ACT OF 1958

NASA SCIENTIFIC AND TECHNICAL PUBLICATIONS

TECHNICAL REPORTS: Scientific and technical information considered important, complete, and a lasting contribution to existing knowledge.

TECHNICAL NOTES: Information less broad in scope but nevertheless of importance as a contribution to existing knowledge.

TECHNICAL MEMORANDUMS: Information receiving limited distribution because of preliminary data, security classification, or other reasons.

CONTRACTOR REPORTS: Technical information generated in connection with a NASA contract or grant and released under NASA auspices.

TECHNICAL TRANSLATIONS: Information published in a foreign language considered to merit NASA distribution in English.

TECHNICAL REPRINTS: Information derived from NASA activities and initially published in the form of journal articles.

SPECIAL PUBLICATIONS: Information derived from or of value to NASA activities but not necessarily reporting the results of individual NASA-programmed scientific efforts. Publications include conference proceedings, monographs, data compilations, handbooks, sourcebooks, and special bibliographies.

Details on the availability of these publications may be obtained from:

SCIENTIFIC AND TECHNICAL INFORMATION DIVISION

NATIONAL AERONAUTICS AND SPACE ADMINISTRATION

Washington, D.C. 20546